Report

Current Biology

Locomotor and olfactory responses in dopamine neurons of the *Drosophila* superior-lateral brain

Highlights

- Specific dopamine neurons connect olfactory regions to locomotor networks
- Activity in these dopamine neurons is locked to spontaneous changes in walking speed
- Some of these cells respond to odors, but repeated stimuli suppress their responses
- The same cell can encode variable sensory-motor combinations in different individuals

Authors

Michael Marquis, Rachel I. Wilson

Correspondence

rachel_wilson@hms.harvard.edu

In brief

Marquis and Wilson describe the physiology of three types of dopamine neurons in the *Drosophila* brain. They show that all these neurons are correlated with the fly's walking speed, and some also respond to odor stimuli. The same identifiable dopamine neuron can encode different combinations of locomotion and odor in different individuals.

Marquis & Wilson, 2022, Current Biology *32*, 5406–5414
December 19, 2022
https://doi.org/10.1016/j.cub.2022.11.008

CellPress

CellPress
OPEN ACCESS

Current Biology

Report

Locomotor and olfactory responses in dopamine neurons of the *Drosophila* superior-lateral brain

Michael Marquis[1] and Rachel I. Wilson[1,2,*]
[1]Department of Neurobiology, Harvard Medical School, 220 Longwood Avenue, Boston, MA 02115, USA
[2]Lead contact
*Correspondence: rachel_wilson@hms.harvard.edu
https://doi.org/10.1016/j.cub.2022.11.008

SUMMARY

The *Drosophila* brain contains about 50 distinct morphological types of dopamine neurons.[1–4] Physiological studies of *Drosophila* dopamine neurons have been largely limited to one brain region, the mushroom body,[5–13] where they are implicated in learning.[14–18] By comparison, we know little about the physiology of other *Drosophila* dopamine neurons. Interestingly, a recent whole-brain imaging study found that dopamine neuron activity in several fly brain regions is correlated with locomotion.[19] This is notable because many dopamine neurons in the rodent brain are also correlated with locomotion or other movements[20–30]; however, most rodent studies have focused on learned and rewarded behaviors, and few have investigated dopamine neuron activity during spontaneous (self-timed) movements. In this study, we monitored dopamine neurons in the *Drosophila* brain during self-timed locomotor movements, focusing on several previously uncharacterized cell types that arborize in the superior-lateral brain, specifically the lateral horn and superior-lateral protocerebrum. We found that activity of all of these dopamine neurons correlated with spontaneous fluctuations in walking speed, with different cell types showing different speed correlations. Some dopamine neurons also responded to odors, but these responses were suppressed by repeated odor encounters. Finally, we found that the same identifiable dopamine neuron can encode different combinations of locomotion and odor in different individuals. If these dopamine neurons promote synaptic plasticity—like the dopamine neurons of the mushroom body—then, their tuning profiles would imply that plasticity depends on a flexible integration of sensory signals, motor signals, and recent experience.

RESULTS

Dopamine neuron morphology and connectivity

The mushroom body is a site of olfactory learning in *Drosophila*, whereas the lateral horn (LH) has long been assumed to mediate innate olfactory behaviors.[31] However, like the mushroom body,[2] the LH is innervated by multiple types of dopamine neurons,[3,32] suggesting that dopamine may modulate olfactory processing in this region, similar to its role in the mushroom body. To better understand dopamine's function in the LH, we investigated three dopamine neuron types (PPM1/2-1, PPL2-1, and PPL2-3). Collectively, these neurons tile the full volume of the LH, together with the superior-lateral protocerebrum (SLP), an adjacent olfactory region.

The hemibrain connectome[33] contains two PPM1/2-1 neurons, one PPL2-1 neuron, and one PPL2-3 neuron in the right hemisphere. Each of these neurons arborizes in several brain regions (Figures 1A–1F), without an obvious division of the cell into axon and dendrite (Table S1). Each of these neurons has a large number of synaptic partners (Figures 1J and 1K; Table S2), but their connectivity is nonetheless selective (Figure S1). For example, the connectome shows that PPM1/2-1 neurons (Figure 1G) receive input from an ascending neuron that carries locomotor signals from the ventral nerve cord,[34] and they provide output to a specific descending neuron that projects to the leg-control regions of the ventral nerve cord.[35,36] They are also reciprocally connected with the mushroom body output neuron that has the strongest direct connections to descending neurons (MBON20).[37] Finally, they are reciprocally connected with specific olfactory local neurons in the antennal lobe. This connectivity pattern predicts that PPM1/2-1 activity is recruited by locomotion and odor.

Meanwhile, PPL2-1 neurons (Figure 1H) receive input from MBON20 as well as several other MBONs. They are reciprocally connected to several LH centrifugal neurons[36] as well as LH output neurons. Interestingly, they are also reciprocally connected to an octopaminergic neuron which is downstream of locomotor-related neurons in the central complex.[38,39] Finally, they send output to several types of Kenyon cells in the mushroom body calyx. This connectivity pattern predicts that PPL2-1 is recruited by odor and locomotion.

Finally, PPL2-3 neurons (Figure 1I) are downstream of LH centrifugal neurons as well as LH output neurons. They also receive direct input from olfactory projection neurons of the antennal lobe. They send output to mushroom body Kenyon cells in the dorsal accessory calyx.[37] This connectivity pattern predicts that PPL2-3 is recruited mainly by sensory input.

Dopamine neuron locomotor responses

The distinct patterns of connectivity in these dopamine neurons motivated us to ask whether they also have distinct functional

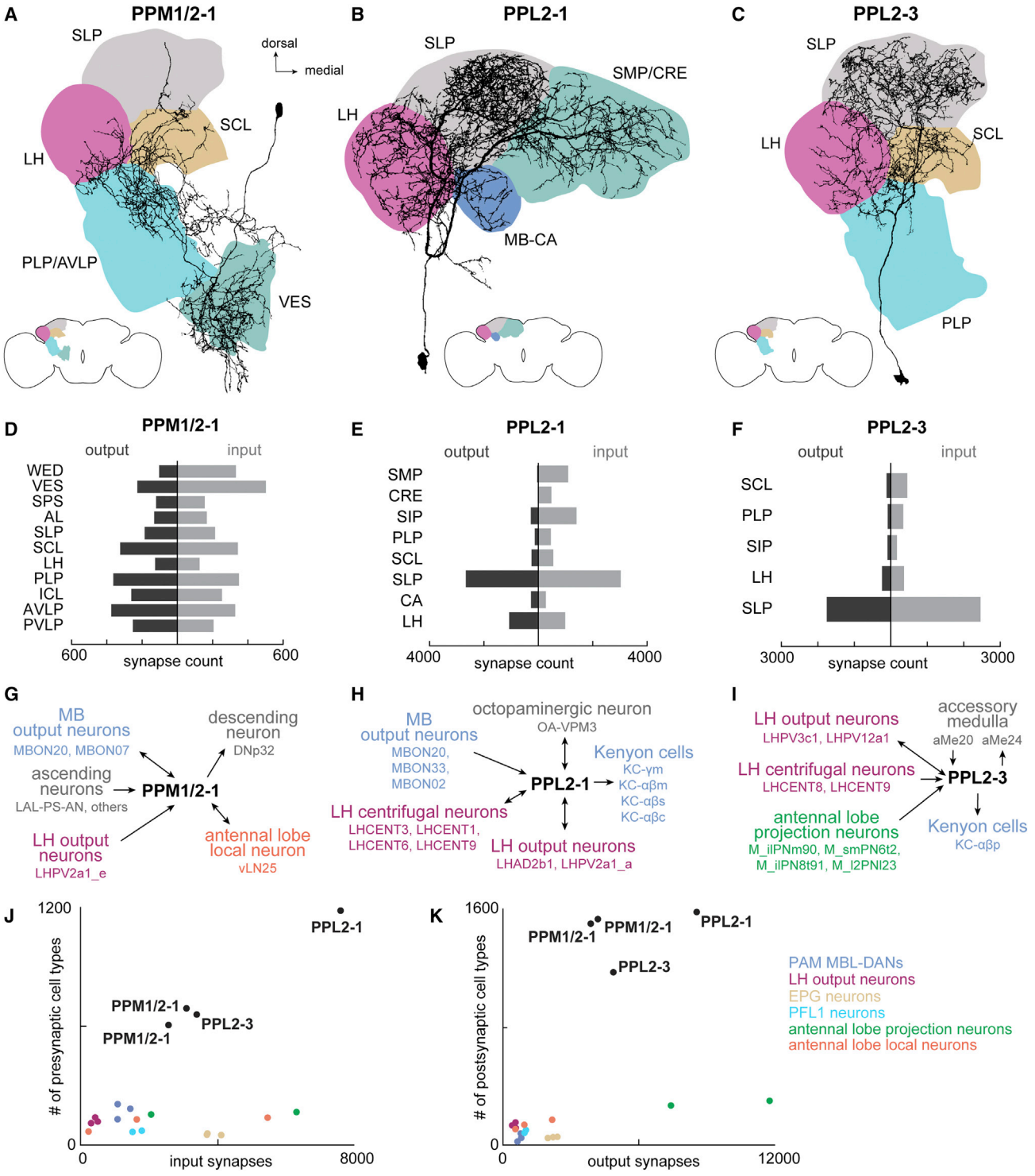

Figure 1. Dopamine neuron morphology and connectivity

(A–C) Morphology of each dopamine neuron type in the hemibrain:v1.2 dataset, with outlines of key brain regions. For brain region abbreviations, see Table S2 or https://neuprint.janelia.org/.

(D–F) Number of pre- and post-synaptic connections formed by each dopamine neuron type in every brain region that contains at least 100 synapses, sorted by input/output ratio. Synapse counts are averaged for the two PPM1/2-1 neurons.

(G–I) Selected synaptic partners of each dopamine neuron type.

(legend continued on next page)

properties. Therefore, we expressed GCaMP in each cell type and monitored their activity using two-photon imaging while flies walked on a spherical treadmill (Figure 2A). We found that the activity of all three cell types increased just after the fly started to walk (Figures 2B–2D). These locomotor onset signals were significantly larger in PPM1/2-1 compared with the other two cell types (Figure 2C).

Moreover, these dopamine neurons continued to be active as flies walked, and we noticed that they tracked the spontaneous fluctuations in the fly's walking speed (Figures 2E and 2F). Overall, the relationship between neural activity (ΔF/F) and walking speed was significantly stronger for PPM1/2-1 compared with the other two cell types (Figures 2G and S2). Changes in neural activity lagged changes in speed by about 300 ms (Figure S2), suggesting that these neurons are responding to speed changes rather than driving those changes. Note that LH/SLP dopamine neurons seem to be specifically locked to locomotion, as they are not active during non-locomotor leg movements (Figure S3). It is interesting that PPL2-1 and PPL2-3 have equally strong locomotor responses, given that the major inputs to PPL2-3 do not arise from brain regions generally associated with locomotion (Figure 1I).

Interestingly, we observed considerable individual variation in locomotor responses. In particular, PPM1/2-1 neurons had strong locomotor responses in some individuals, whereas in other individuals, they had much weaker responses (Figures 2D, 2G, and S2). Thus, locomotor input to these neurons appears to be flexible.

Dopamine neuron odor responses

Next, we investigated whether these dopamine neurons respond to odor stimuli (Figure 3A). We focused on appetitive stimuli (ethanol and vinegar) because some of the neurons in these dopamine cell clusters have been linked to appetitive behaviors.[40–43] Unexpectedly, we found that the cell type with the strongest locomotor-related activity (PPM1/2-1) almost never responded to these odors, either in whole-cell recordings (Figure 3A) or in imaging experiments from locomoting flies (Figure 3B). Only in one experiment did this cell type respond to odor, and this response was relatively weak (Figure 3B). By contrast, the second cell type (PPL2-1) was consistently excited by odor. This was true in whole-cell recordings (Figure 3C) as well as imaging experiments in locomoting flies (Figure 3D). The last cell type, PPL2-3, also responded to odors: in whole-cell recordings, when flies were quiescent, it was typically inhibited at odor onset and excited at odor offset (Figure 3E). However, in calcium imaging experiments in locomoting flies, PPL2-3 odor responses had more diverse dynamics, with more individual variation and odor-dependent variation (Figures 3G and 3F).

These results illustrate how difficult it can be to predict a cell's tuning based on connectome data. On one hand, PPM1/2-1 is generally unresponsive to odors, although its top input is an olfactory mushroom body output neuron (MBON20).[37] On the other hand, PPL2-3 has highly individualized odor responses, although it receives almost no direct MBON input, and MBONs are the cells within the olfactory system where individual variations have been most clearly documented.[11,44] Thus, the anatomical inputs to these dopamine neurons might be regarded as flexible rather than fixed.

Locomotor and olfactory contributions to dopamine neuron dynamics

Thus far, we have seen that dopamine neuron activity can depend on both locomotion and odor. To quantify the relative contributions of these factors, we fit a linear regression to each cell's activity pattern. These models allowed us to compactly summarize and compare the properties of different cells, both within and across cell types.

First, we found that the fly's walking speed explained a remarkable amount of the variance in PPM1/2-1 activity (Figures 4A and 4B), with R^2 values approaching 0.6 in many individuals. Including the odor stimulus in the linear regression produced no improvement in the fit, except in the one individual that had obvious odor responses. This result supports our conclusion that PPM1/2-1 dopamine neurons are primarily locomotor-related.

Next, we turned to the two other dopamine neuron types (PPL2-1 and PPL2-3), whose properties are more complicated. Both these cell types respond to combinations of walking speed and odor, with the latter cell type often showing both excitation and inhibition in response to a single odor pulse. Interestingly, in some individuals, we noticed that the odor responses of these cells were suppressed by repeated odor presentations (Figures 4C–4E). We could accelerate this suppression by switching to a high odor pulse rate (Figures 4C and 4D).

To model the odor responses of these cells, we first computed each cell's average response to an odor pulse. Then, we caused odor responses to decrement by a certain fraction with every odor pulse, recovering with an exponential time course; the fractional decrement per pulse was fit as a free parameter in each cell, with uniform recovery dynamics for all cells. Adding this type of odor response suppression to the model allowed us to capture much of the odor response variation in many cells (Figures 4F and 4G).

We also noticed that the onset of the high odor pulse frequency caused a downward shift in baseline fluorescence in some experiments (Figure 4D). We therefore augmented the model with subtractive inhibition that appears with each odor pulse and decays exponentially over time. Adding this component further improved the model fit in some cells (Figures 4F and 4G).

Interestingly, we found that dopamine neuron odor responses evolved with different dynamics in different individuals. In some individuals, we found clear evidence of odor response suppression and/or subtractive inhibition

(J) Number of upstream cell types versus total number of input synapses for each dopamine neuron type, along with a variety of other cell types for comparison. Each point represents a single neuron and is colored-coded by cell type.
(K) Equivalent plot for downstream connectivity.
See also Figure S1 and Tables S1 and S2.

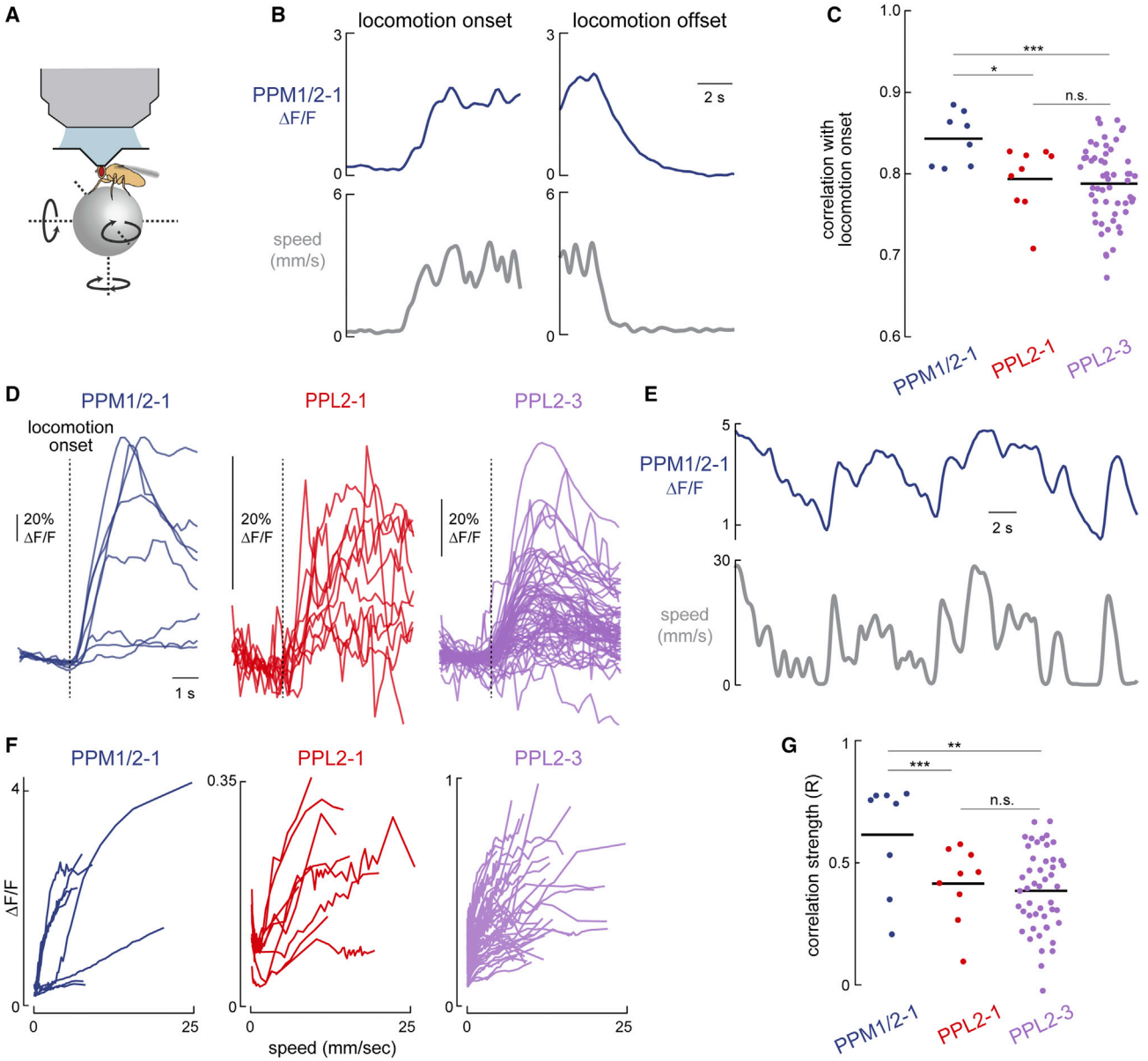

Figure 2. Dopamine neuron locomotor responses

(A) Schematic showing experimental design.

(B) Example of PPM1/2-1 activity at locomotion onset and offset.

(C) Peak cross-correlation coefficient between ΔF/F and translational (*xy*) walking speed after locomotion onset. Each symbol is the mean for one fly. Black lines signify the mean for each cell type (*$p < 0.05$, **$p < 0.01$, one-way ANOVA with Tukey HSD post hoc test and Fisher Z-transform; n = 8 for PPM1/2, 9 for PPL2-1, and 48 for PPL2-3 in C, D, F, and G).

(D) Event-averaged GCaMP responses at the onset of walking bouts. Each trace is the mean for one fly.

(E) Example of PPM1/2-1 tracking walking speed.

(F) Mean ΔF/F versus walking speed for PPM1/2-1, PPL2-3, and PPL2-1. Each line represents the mean for one fly.

(G) Pearson correlation between ΔF/F and walking speed. Each point is one fly (**$p < 0.01$, ***$p < 0.001$, one-way ANOVA with Tukey HSD post hoc test and Fisher Z-transform).

See also Figures S2 and S3.

(Figure 4G), whereas there was no indication of suppression or inhibition in other individuals. Our results suggest that all these dopamine neurons have access to speed and odor information, but these variables are weighted differently in different cell types and individuals.

DISCUSSION

Here, we describe three types of dopamine neurons that collectively tile the superior-lateral brain. They are all part of the TH-C′ group,[9] whose activity promotes food-dwelling

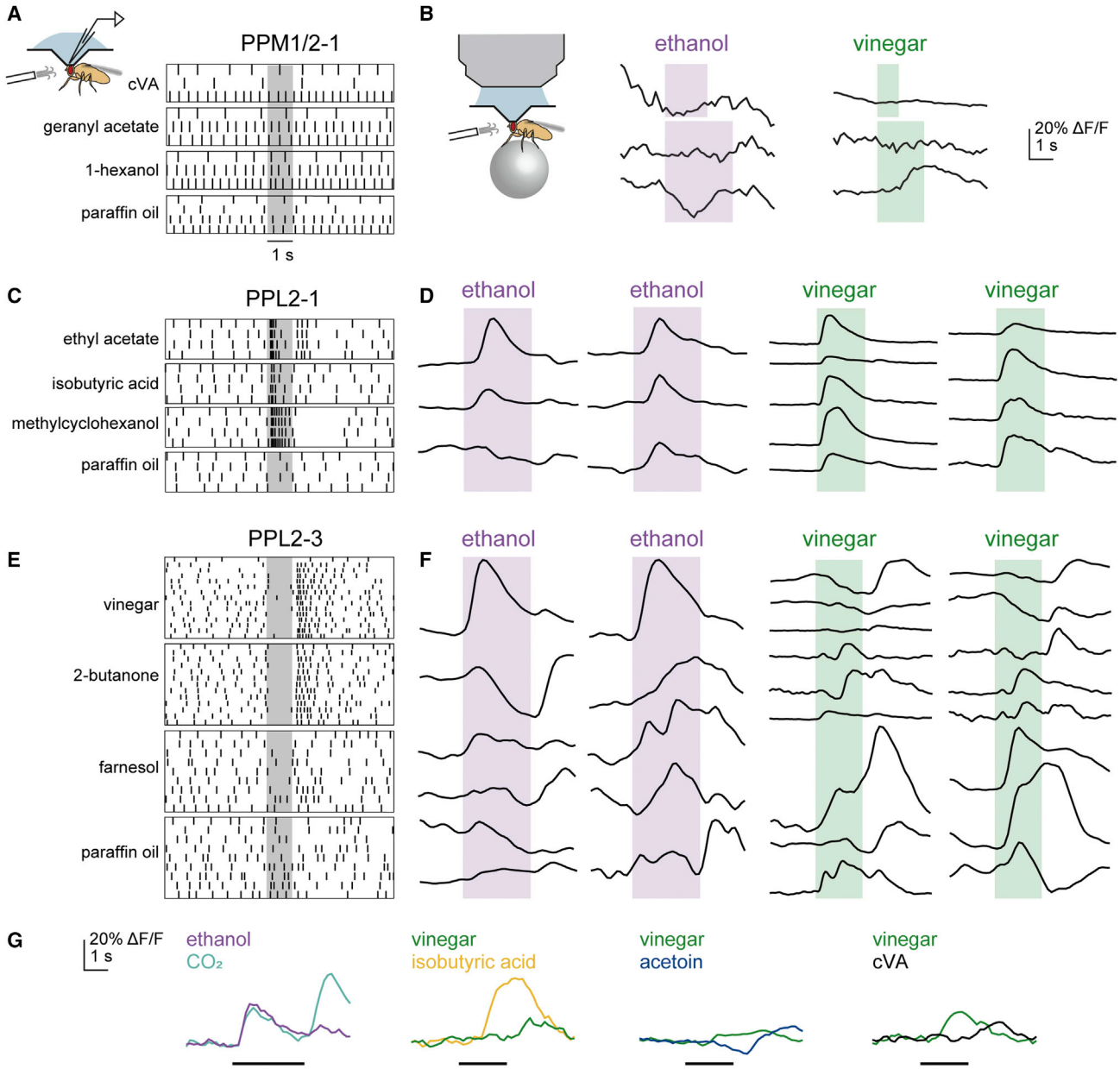

Figure 3. Dopamine neuron odor responses

(A) Spike rasters showing responses of one example PPM1/2-1 neuron to three different odors and a solvent control (paraffin oil) during whole-cell recording. Shading indicates odor delivery (cVA, *cis*-vaccenyl acetate).

(B) PPM1/2-1 GCaMP responses (ΔF/F) to ethanol or vinegar. Each trace shows the trial-averaged response for one individual (6 flies total). Only trials when the fly was not walking were included.

(C and D) Same but for PPL2-1. Each trace in (D) is from a different fly (n = 15 total).

(E and F) Same but for PPL2-3. Each trace in (F) is from a different fly (n = 29 total).

(G) Trial-averaged responses of four PPL2-3 neurons to two different odors presented in interleaved trials. Each pair of traces shows data from an individual fly.

behavior[40] and causes females to choose sucrose-rich locations for egg-laying.[41] In particular, the PPL2 cluster within the TH-C′ group facilitates odor responses in mushroom body Kenyon cells[45] and promotes male courtship behavior,[42,43] which has a large olfactory component. Together, these findings suggest a general role in appetitive behaviors.

Notably, we show that one of these cell types (PPM1/2-1) is highly correlated with rapid spontaneous fluctuations in walking speed. This is reminiscent of some dopamine neurons in the *Drosophila* mushroom body lobes, which are correlated with locomotion or leg movement.[5,11,12,13] Similarly, in the rodent brain, some dopamine neurons correlate with forward acceleration of the body or rotational velocity of the head.[20–30]

CellPress
OPEN ACCESS

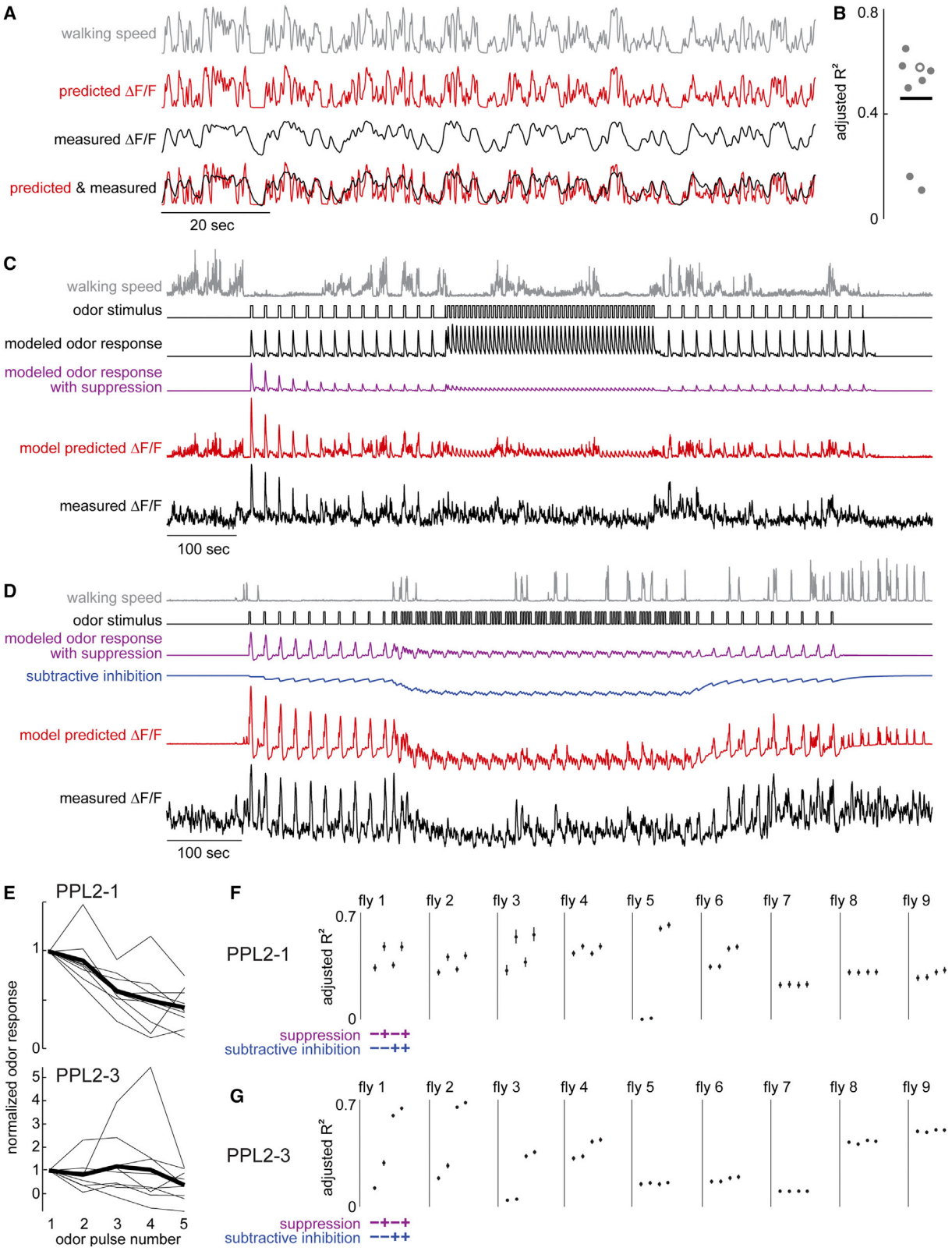

Figure 4. Locomotor and olfactory contributions to dopamine neuron dynamics

(A) One example PPM1/2-1 imaging session. Walking speed was used to predict ΔF/F.

(B) Variance explained by linear models fit to PPM1/2-1 for each experiment (adjusted R^2). Black line is the mean (n = 8 flies). Open circle is the example from (A).

(legend continued on next page)

The dopamine neurons we describe here track locomotor speed with a lag; this suggests that these neurons are not controlling locomotor speed. Rather, these neurons may promote learning about the consequences of speed changes. For example, dopamine could serve as a "when-to-learn" signal that modifies the rate of associative synaptic plasticity.[32] Locking dopamine to locomotion could be a way to accelerate learning when the organism is moving through the environment, and thus, new information is likely to be available (unpublished data).[46]

We also found odor responses in some of these dopamine neurons, akin to the odor responses in many mushroom body dopamine neurons.[3,47–51] Notably, we found that odor responses in PPL2-1 and PPL2-3 neurons were suppressed by repeated odor encounters. The same type of suppression has been shown previously for a specific mushroom body dopamine neuron (PPL1-4, also known as PPL-α'3).[52] Because odor response suppression is quite variable across individuals, it is unlikely to be purely due to peripheral adaptation.[53,54] Interestingly, some dopamine neurons in the mammalian brain also respond preferentially to unexpected or novel stimuli.[55–61] If dopamine functions as a generalized when-to-learn signal, it is logical that dopamine should be linked to novelty. Experience-dependent suppression of dopamine neuron sensory responses may be due to feedback loops that allow these dopamine neurons to monitor the activity of their target cells.[2,36,62–65]

A notable feature of these neurons is their inter-individual variability. This stands in contrast to many other neurons in the LH and/or SLP, which tend to have fairly stereotyped functional properties.[66,67] Rather, it is more similar to physiology of mushroom body dopamine neurons, which have plastic odor responses.[5,50–52]

In the future, it will be interesting to determine how these dopamine neurons influence appetitive olfactory behaviors. Our results predict that the learned aspects of these behaviors will depend on the fly's locomotor state: faster locomotion should promote more dopamine release and thus faster learning. This might be a way to facilitate learning when a fly is exploring a new environment.

STAR★METHODS

Detailed methods are provided in the online version of this paper and include the following:

- KEY RESOURCES TABLE
- RESOURCE AVAILABILITY
  - Lead contact
  - Materials availability
  - Data and code availability
- EXPERIMENTAL MODEL AND SUBJECT DETAILS
  - Fly husbandry and genotypes
  - Fly preparation and dissection
- METHOD DETAILS
  - Patch-clamp recordings
  - Two-photon calcium imaging
  - Measurement of fly locomotion
  - Delivery of odor stimuli
- QUANTIFICATION AND STATISTICAL ANALYSIS
  - Calcium imaging alignment and processing
  - Electrophysiology spike detection
  - Morphology and connectomics analysis
  - Locomotion data processing
  - Modeling PPM1/2-1 activity
  - Modeling PPL2-1 and PPL2-3 activity

SUPPLEMENTAL INFORMATION

Supplemental information can be found online at https://doi.org/10.1016/j.cub.2022.11.008.

ACKNOWLEDGMENTS

We thank Greg Jefferis, Alexander Bates, Quinn Vanderbeck, and Peter Gibb for assistance in pilot connectome analyses. Michael Dickinson provided styrofoam balls. Margaret Ho, Mark Wu, Barret Pfeiffer, and Gerry Rubin donated fly stocks. Stephen Holtz advised on modeling analyses. Members of the Wilson lab provided feedback on the manuscript. We received funding from the NIH (R01 DC008174 and U19 NS104655 to R.I.W. and F31 DC016471 to M.M.) and HHMI (Investigator funding to R.I.W.). This work was supported by the Bloomington Drosophila Stock Center (NIH P40 OD018537), the Harvard Medical School Neurobiology Imaging Facility (NIH P30 NS072030), and the HMS Research Instrumentation Core Facility.

AUTHOR CONTRIBUTIONS

M.M. performed all experiments and all analyses. M.M. and R.I.W. designed the study and wrote the manuscript.

DECLARATION OF INTERESTS

The authors declare no competing interests.

Received: June 24, 2022
Revised: August 17, 2022
Accepted: November 3, 2022
Published: November 29, 2022

REFERENCES

1. Hartenstein, V., Cruz, L., Lovick, J.K., and Guo, M. (2017). Developmental analysis of the dopamine-containing neurons of the *Drosophila* brain. J. Comp. Neurol. *525*, 363–379.
2. Aso, Y., Hattori, D., Yu, Y., Johnston, R.M., Iyer, N.A., Ngo, T.T., Dionne, H., Abbott, L.F., Axel, R., Tanimoto, H., and Rubin, G.M. (2014). The

(C) One example PPL2-1 imaging session. The "modeled odor response" is the average response to an odor pulse; to generate the "modeled odor response with suppression," we let the response decrement by some fraction with every pulse, recovering with an exponential time course. This was then used, along with walking speed, to predict $\Delta F/F$.
(D) Same as (C), but for an example PPL2-3 experiment. Here, the regression includes subtractive inhibition that grows with pulse frequency.
(E) Change in odor response magnitude for the first five odor pulses in each of the PPL2-1 and PPL2-3 experiments. Each point represents the peak $\Delta F/F$ during the 2-sec window after odor onset, relative to the first response. Gray lines are individual flies and black lines are the mean.
(F) Predictive performance of PPL2-1 model variants. In each variant, we used walking speed and modeled odor response as predictive variables. Each range shows bootstrapped 95% confidence intervals for R^2 values when evaluated on a randomly held out 20% test set of the data. Fly 1 is shown in (C).
(G) Same as (F) but for PPL2-3 experiments. Fly 1 is shown in (D).

neuronal architecture of the mushroom body provides a logic for associative learning. eLife *3*, e04577.

3. Mao, Z., and Davis, R.L. (2009). Eight different types of dopaminergic neurons innervate the *Drosophila* mushroom body neuropil: anatomical and physiological heterogeneity. Front. Neural Circuits *3*, 5.
4. Xie, T., Ho, M.C.W., Liu, Q., Horiuchi, W., Lin, C.-C., Task, D., Luan, H., White, B.H., Potter, C.J., and Wu, M.N. (2018). A genetic toolkit for dissecting dopamine circuit function in *Drosophila*. Cell Rep. *23*, 652–665.
5. Zolin, A., Cohn, R., Pang, R., Siliciano, A.F., Fairhall, A.L., and Ruta, V. (2021). Context-dependent representations of movement in *Drosophila* dopaminergic reinforcement pathways. Nat. Neurosci. *24*, 1555–1566.
6. Tomchik, S.M. (2013). Dopaminergic neurons encode a distributed, asymmetric representation of temperature in *Drosophila*. J. Neurosci. *33*, 2166–2176.
7. Das, G., Klappenbach, M., Vrontou, E., Perisse, E., Clark, C.M., Burke, C.J., and Waddell, S. (2014). *Drosophila* learn opposing components of a compound food stimulus. Curr. Biol. *24*, 1723–1730.
8. Galili, D.S., Dylla, K.V., Lüdke, A., Friedrich, A.B., Yamagata, N., Wong, J.Y.H., Ho, C.H., Szyszka, P., and Tanimoto, H. (2014). Converging circuits mediate temperature and shock aversive olfactory conditioning in *Drosophila*. Curr. Biol. *24*, 1712–1722.
9. Liu, C., Plaçais, P.Y., Yamagata, N., Pfeiffer, B.D., Aso, Y., Friedrich, A.B., Siwanowicz, I., Rubin, G.M., Preat, T., and Tanimoto, H. (2012). A subset of dopamine neurons signals reward for odour memory in *Drosophila*. Nature *488*, 512–516.
10. Tsao, C.H., Chen, C.C., Lin, C.H., Yang, H.Y., and Lin, S. (2018). *Drosophila* mushroom bodies integrate hunger and satiety signals to control innate food-seeking behavior. eLife *7*, e35264. https://doi.org/10.7554/eLife.35264.
11. Cohn, R., Morantte, I., and Ruta, V. (2015). Coordinated and compartmentalized neuromodulation shapes sensory processing in *Drosophila*. Cell *163*, 1742–1755.
12. Berry, J.A., Cervantes-Sandoval, I., Chakraborty, M., and Davis, R.L. (2015). Sleep facilitates memory by blocking dopamine neuron-mediated forgetting. Cell *161*, 1656–1667.
13. Siju, K.P., Štih, V., Aimon, S., Gjorgjieva, J., Portugues, R., and Grunwald Kadow, I.C. (2020). Valence and state-dependent population coding in dopaminergic neurons in the fly mushroom body. Curr. Biol. *30*, 2104–2115.e4.
14. Modi, M.N., Shuai, Y., and Turner, G.C. (2020). The *Drosophila* mushroom body: from architecture to algorithm in a learning circuit. Annu. Rev. Neurosci. *43*, 465–484.
15. Adel, M., and Griffith, L.C. (2021). The role of dopamine in associative learning in *Drosophila*: an updated unified model. Neurosci. Bull. *37*, 831–852.
16. Boto, T., Stahl, A., and Tomchik, S.M. (2020). Cellular and circuit mechanisms of olfactory associative learning in *Drosophila*. J. Neurogenet. *34*, 36–46.
17. Siju, K.P., De Backer, J.-F., and Grunwald Kadow, I.C. (2021). Dopamine modulation of sensory processing and adaptive behavior in flies. Cell Tissue Res. *383*, 207–225.
18. Waddell, S. (2013). Reinforcement signalling in *Drosophila*; dopamine does it all after all. Curr. Opin. Neurobiol. *23*, 324–329.
19. Aimon, S., Katsuki, T., Jia, T., Grosenick, L., Broxton, M., Deisseroth, K., Sejnowski, T.J., and Greenspan, R.J. (2019). Fast near-whole-brain imaging in adult *Drosophila* during responses to stimuli and behavior. PLoS Biol. *17*, e2006732.
20. Puryear, C.B., Kim, M.J., and Mizumori, S.J.Y. (2010). Conjunctive encoding of movement and reward by ventral tegmental area neurons in the freely navigating rodent. Behav. Neurosci. *124*, 234–247.
21. Wang, D.V., and Tsien, J.Z. (2011). Conjunctive processing of locomotor signals by the ventral tegmental area neuronal population. PLoS One *6*, e16528.
22. Barter, J.W., Li, S., Lu, D., Bartholomew, R.A., Rossi, M.A., Shoemaker, C.T., Salas-Meza, D., Gaidis, E., and Yin, H.H. (2015). Beyond reward prediction errors: the role of dopamine in movement kinematics. Front. Integr. Neurosci. *9*, 39.
23. Dodson, P.D., Dreyer, J.K., Jennings, K.A., Syed, E.C.J., Wade-Martins, R., Cragg, S.J., Bolam, J.P., and Magill, P.J. (2016). Representation of spontaneous movement by dopaminergic neurons is cell-type selective and disrupted in parkinsonism. Proc. Natl. Acad. Sci. USA *113*, E2180–E2188.
24. Coddington, L.T., and Dudman, J.T. (2018). The timing of action determines reward prediction signals in identified midbrain dopamine neurons. Nat. Neurosci. *21*, 1563–1573.
25. da Silva, J.A., Tecuapetla, F., Paixão, V., and Costa, R.M. (2018). Dopamine neuron activity before action initiation gates and invigorates future movements. Nature *554*, 244–248.
26. Engelhard, B., Finkelstein, J., Cox, J., Fleming, W., Jang, H.J., Ornelas, S., Koay, S.A., Thiberge, S.Y., Daw, N.D., Tank, D.W., and Witten, I.B. (2019). Specialized coding of sensory, motor and cognitive variables in VTA dopamine neurons. Nature *570*, 509–513.
27. Lee, R.S., Mattar, M.G., Parker, N.F., Witten, I.B., and Daw, N.D. (2019). Reward prediction error does not explain movement selectivity in DMS-projecting dopamine neurons. eLife *8*, e42992. https://doi.org/10.7554/eLife.42992.
28. Kremer, Y., Flakowski, J., Rohner, C., and Lüscher, C. (2020). Context-dependent multiplexing by individual VTA dopamine neurons. J. Neurosci. *40*, 7489–7509.
29. Hughes, R.N., Bakhurin, K.I., Petter, E.A., Watson, G.D.R., Kim, N., Friedman, A.D., and Yin, H.H. (2020). Ventral tegmental dopamine neurons control the impulse vector during motivated behavior. Curr. Biol. *30*, 2681–2694.e5.
30. Moss, M.M., Zatka-Haas, P., Harris, K.D., Carandini, M., and Lak, A. (2021). Dopamine axons in dorsal striatum encode contralateral visual stimuli and choices. J. Neurosci. *41*, 7197–7205.
31. Masse, N.Y., Turner, G.C., and Jefferis, G.S. (2009). Olfactory information processing in *Drosophila*. Curr. Biol. *19*, R700–R713.
32. Frémaux, N., and Gerstner, W. (2015). Neuromodulated spike-timing-dependent plasticity, and theory of three-factor learning rules. Front. Neural Circuits *9*, 85.
33. Scheffer, L.K., Xu, C.S., Januszewski, M., Lu, Z., Takemura, S.Y., Hayworth, K.J., Huang, G.B., Shinomiya, K., Maitlin-Shepard, J., Berg, S., et al. (2020). A connectome and analysis of the adult *Drosophila* central brain. eLife *9*, e57443. https://doi.org/10.7554/eLife.57443.
34. Fujiwara, T., Brotas, M., and Chiappe, M.E. (2022). Walking strides direct rapid and flexible recruitment of visual circuits for course control in *Drosophila*. Neuron *110*, 2124–2138.e8. https://doi.org/10.1016/j.neuron.2022.04.008.
35. Namiki, S., Dickinson, M.H., Wong, A.M., Korff, W., and Card, G.M. (2018). The functional organization of descending sensory-motor pathways in *Drosophila*. eLife *7*, e34272.
36. Schlegel, P., Bates, A.S., Stürner, T., Jagannathan, S.R., Drummond, N., Hsu, J., Serratosa Capdevila, L., Javier, A., Marin, E.C., Barth-Maron, A., et al. (2021). Information flow, cell types and stereotypy in a full olfactory connectome. eLife *10*, e66018. https://doi.org/10.7554/eLife.66018.
37. Li, F., Lindsey, J.W., Marin, E.C., Otto, N., Dreher, M., Dempsey, G., Stark, I., Bates, A.S., Pleijzier, M.W., Schlegel, P., et al. (2020). The connectome of the adult *Drosophila* mushroom body provides insights into function. eLife *9*, e62576. https://doi.org/10.7554/eLife.62576.
38. Lu, J., Behbahani, A.H., Hamburg, L., Westeinde, E.A., Dawson, P.M., Lyu, C., Maimon, G., Dickinson, M.H., Druckmann, S., and Wilson, R.I. (2022). Transforming representations of movement from body- to world-centric space. Nature *601*, 98–104.
39. Lyu, C., Abbott, L.F., and Maimon, G. (2021). A neuronal circuit for vector computation builds an allocentric traveling-direction signal in the *Drosophila* fan-shaped body. Nature *601*, 92–97.

40. Landayan, D., Feldman, D.S., and Wolf, F.W. (2018). Satiation state-dependent dopaminergic control of foraging in *Drosophila*. Sci. Rep. *8*, 5777.

41. Yang, C.H., He, R., and Stern, U. (2015). Behavioral and circuit basis of sucrose rejection by *Drosophila* females in a simple decision-making task. J. Neurosci. *35*, 1396–1410.

42. Chen, S.L., Chen, Y.H., Wang, C.C., Yu, Y.W., Tsai, Y.C., Hsu, H.W., Wu, C.L., Wang, P.Y., Chen, L.C., Lan, T.H., and Fu, T.-F. (2017). Active and passive sexual roles that arise in *Drosophila* male-male courtship are modulated by dopamine levels in PPL2ab neurons. Sci. Rep. *7*, 44595.

43. Kuo, S.Y., Wu, C.L., Hsieh, M.Y., Lin, C.T., Wen, R.K., Chen, L.C., Chen, Y.H., Yu, Y.W., Wang, H.D., Su, Y.J., et al. (2015). PPL2ab neurons restore sexual responses in aged *Drosophila* males through dopamine. Nat. Commun. *6*, 7490.

44. Hige, T., Aso, Y., Modi, M.N., Rubin, G.M., and Turner, G.C. (2015). Heterosynaptic plasticity underlies aversive olfactory learning in *Drosophila*. Neuron *88*, 985–998.

45. Boto, T., Stahl, A., Zhang, X., Louis, T., and Tomchik, S.M. (2019). Independent contributions of discrete dopaminergic circuits to cellular plasticity, memory strength, and valence in *Drosophila*. Cell Rep. *27*, 2014–2021.e2.

46. Kim, S.S., Hermundstad, A.M., Romani, S., Abbott, L.F., and Jayaraman, V. (2019). Generation of stable heading representations in diverse visual scenes. Nature *576*, 126–131.

47. Vrontou, E., Groschner, L.N., Szydlowski, S., Brain, R., Krebbers, A., and Miesenböck, G. (2021). Response competition between neurons and antineurons in the mushroom body. Curr. Biol. *31*, 4911–4922.e4.

48. Jacob, P.F., and Waddell, S. (2020). Spaced training forms complementary long-term memories of opposite valence in *Drosophila*. Neuron *106*, 977–991.e4. https://doi.org/10.1016/j.neuron.2020.03.013.

49. Jacob, P.F., Vargas-Gutierrez, P., Okray, Z., Vietti-Michelina, S., Felsenberg, J., and Waddell, S. (2021). Prior experience conditionally inhibits the expression of new learning in *Drosophila*. Curr. Biol. *31*, 3490–3503.e3.

50. McCurdy, L.Y., Sareen, P., Davoudian, P.A., and Nitabach, M.N. (2021). Dopaminergic mechanism underlying reward-encoding of punishment omission during reversal learning in *Drosophila*. Nat. Commun. *12*, 1115.

51. Dylla, K.V., Raiser, G., Galizia, C.G., and Szyszka, P. (2017). Trace conditioning in *Drosophila* induces associative plasticity in mushroom body kenyon cells and dopaminergic neurons. Front. Neural Circuits *11*, 42.

52. Hattori, D., Aso, Y., Swartz, K.J., Rubin, G.M., Abbott, L.F., and Axel, R. (2017). Representations of novelty and familiarity in a mushroom body compartment. Cell *169*, 956–969.e17.

53. Das, S., Sadanandappa, M.K., Dervan, A., Larkin, A., Lee, J.A., Sudhakaran, I.P., Priya, R., Heidari, R., Holohan, E.E., Pimentel, A., et al. (2011). Plasticity of local GABAergic interneurons drives olfactory habituation. Proc. Natl. Acad. Sci. USA *108*, E646–E654.

54. Nagel, K.I., and Wilson, R.I. (2011). Biophysical mechanisms underlying olfactory receptor neuron dynamics. Nat. Neurosci. *14*, 208–216.

55. Ljungberg, T., Apicella, P., and Schultz, W. (1992). Responses of monkey dopamine neurons during learning of behavioral reactions. J. Neurophysiol. *67*, 145–163.

56. Horvitz, J.C., Stewart, T., and Jacobs, B.L. (1997). Burst activity of ventral tegmental dopamine neurons is elicited by sensory stimuli in the awake cat. Brain Res. *759*, 251–258.

57. Kakade, S., and Dayan, P. (2002). Dopamine: generalization and bonuses. Neural Netw. *15*, 549–559.

58. Redgrave, P., and Gurney, K. (2006). The short-latency dopamine signal: a role in discovering novel actions? Nat. Rev. Neurosci. *7*, 967–975.

59. Sharpe, M.J., Chang, C.Y., Liu, M.A., Batchelor, H.M., Mueller, L.E., Jones, J.L., Niv, Y., and Schoenbaum, G. (2017). Dopamine transients are sufficient and necessary for acquisition of model-based associations. Nat. Neurosci. *20*, 735–742. https://doi.org/10.1038/nn.4538.

60. Stalnaker, T.A., Howard, J.D., Takahashi, Y.K., Gershman, S.J., Kahnt, T., and Schoenbaum, G. (2019). Dopamine neuron ensembles signal the content of sensory prediction errors. eLife *8*, e49315. https://doi.org/10.7554/eLife.49315.

61. Morrens, J., Aydin, Ç., Janse van Rensburg, A., Esquivelzeta Rabell, J., and Haesler, S. (2020). Cue-evoked dopamine promotes conditioned responding during learning. Neuron *106*, 142–153.e7.

62. Eschbach, C., Fushiki, A., Winding, M., Schneider-Mizell, C.M., Shao, M., Arruda, R., Eichler, K., Valdes-Aleman, J., Ohyama, T., Thum, A.S., et al. (2020). Recurrent architecture for adaptive regulation of learning in the insect brain. Nat. Neurosci. *23*, 544–555.

63. Otto, N., Pleijzier, M.W., Morgan, I.C., Edmondson-Stait, A.J., Heinz, K.J., Stark, I., Dempsey, G., Ito, M., Kapoor, I., Hsu, J., et al. (2020). Input connectivity reveals additional heterogeneity of dopaminergic reinforcement in *Drosophila*. Curr. Biol. *30*, 3200–3211.e8.

64. Pavlowsky, A., Schor, J., Plaçais, P.-Y., and Preat, T. (2018). A GABAergic feedback shapes dopaminergic input on the *Drosophila* mushroom body to promote appetitive long-term memory. Curr. Biol. *28*, 1783–1793.e4.

65. Felsenberg, J., Jacob, P.F., Walker, T., Barnstedt, O., Edmondson-Stait, A.J., Pleijzier, M.W., Otto, N., Schlegel, P., Sharifi, N., Perisse, E., et al. (2018). Integration of parallel opposing memories underlies memory extinction. Cell *175*, 709–722.e15.

66. Jeanne, J.M., Fişek, M., and Wilson, R.I. (2018). The organization of projections from olfactory glomeruli onto higher-order neurons. Neuron *98*, 1198–1213.e6.

67. Frechter, S., Bates, A.S., Tootoonian, S., Dolan, M.-J., Manton, J., Jamasb, A.R., Kohl, J., Bock, D., and Jefferis, G. (2019). Functional and anatomical specificity in a higher olfactory centre. eLife *8*, e44590.

68. Gouwens, N.W., and Wilson, R.I. (2009). Signal propagation in *Drosophila* central neurons. J. Neurosci. *29*, 6239–6249.

69. Moore, R.J.D., Taylor, G.J., Paulk, A.C., Pearson, T., van Swinderen, B., and Srinivasan, M.V. (2014). FicTrac: a visual method for tracking spherical motion and generating fictive animal paths. J. Neurosci. Methods *225*, 106–119.

70. Pnevmatikakis, E.A., and Giovannucci, A. (2017). NoRMCorre: an online algorithm for piecewise rigid motion correction of calcium imaging data. J. Neurosci. Methods *291*, 83–94.

71. Plaza, S.M., Clements, J., Dolafi, T., Umayam, L., Neubarth, N.L., Scheffer, L.K., et al. (2022). neuPrint: an open access tool for EM connectomics. Front. Neuroinform. *16*, 896292. https://doi.org/10.3389/fninf.2022.896292.

72. Schneider, C.A., Rasband, W.S., and Eliceiri, K.W. (2012). NIH Image to ImageJ: 25 years of image analysis. Nat. Methods *9*, 671–675.

73. Bates, A.S., Manton, J.D., Jagannathan, S.R., Costa, M., Schlegel, P., Rohlfing, T., and Jefferis, G.S.X.E. (2020). The natverse, a versatile toolbox for combining and analysing neuroanatomical data. eLife *9*, e53350.

74. Jefferis, A.B.A.G. (2020). hemibrainr: code for working with data from Janelia FlyEM's hemibrain project. https://github.com/natverse/hemibrainr.

75. Tsodyks, M.V., and Markram, H. (1997). The neural code between neocortical pyramidal neurons depends on neurotransmitter release probability. Proc. Natl. Acad. Sci. USA *94*, 719–723.

76. Abbott, L.F., Varela, J.A., Sen, K., and Nelson, S.B. (1997). Synaptic depression and cortical gain control. Science *275*, 220–224.

STAR★METHODS

KEY RESOURCES TABLE

REAGENT or RESOURCE	SOURCE	IDENTIFIER
Experimental models: Organisms/strains		
P{w[+mC]=ple-Gal4.F}3	Bloomington Drosophila Stock Center (BDSC)	RRID: BDSC_8848
PBac{y[+t7.7]w[+mC]=20XUAS-IVS-jGCaMP7f}VK00005	BDSC	RRID: BDSC_79031
76F02-AD #B (attP40)	Mark Wu (Johns Hopkins University)	N/A
TH-D-AD #1	Mark Wu (Johns Hopkins University)	N/A
55C10-DBD #1 (attP2)	Mark Wu (Johns Hopkins University)	N/A
61H03-DBD #1 (attP2)	Mark Wu (Johns Hopkins University)	N/A
TH-C′-Gal4	Mark Wu (Johns Hopkins University)	N/A
TH-G-KZ #1	Mark Wu (Johns Hopkins University)	N/A
P{20XUAS-IVS-mCD8::GFP}attP2	Gerry Rubin (Janelia)	RRID: BDSC_32194
P{20XUAS-IVS-Syn21-opGCaMP6s-P10}su(Hw)attP5	Gerry Rubin (Janelia)	FlyBase: FBti0195669
P{20XUAS-IVS-Syn21-opGCaMP6s-p10}su(Hw)attP1	Gerry Rubin (Janelia)	N/A
{pJFRC7-20XUAS-cyRFP}VK00037	Tom Clandinin (Stanford University)	N/A
Deposited data		
Drosophila hemibrain v.1.2.1	Scheffer et al.[32]	https://neuprint.janelia.org
Software and algorithms		
ScanImage 2018	Vidrio Technologies	N/A
FicTrac	Moore et al.[69]	http://rjdmoore.net/fictrac/
Matlab R2016a, R2017b, and 2019b	MathWorks	N/A
NoRMCorre	N/A	https://github.com/flatironinstitute/NoRMCorre
R	R Foundation for Statistical Computing, Vienna, Austria	https://www.r-project.org/
neuprint	Plaza et al.[71]	https://neuprint.janelia.org
ImageJ 1.52	Schneider et al.[72]	https://imagej.nih.gov/ij/
Data analysis code	This paper	https://github.com/wilson-lab https://doi.org/10.5281/zenodo.7295005

RESOURCE AVAILABILITY

Lead contact

Further information and requests for resources and reagents should be directed to and will be fulfilled by the lead contact, Rachel Wilson (rachel_wilson@hms.harvard.edu).

Materials availability

This study did not generate new unique reagents.

Data and code availability

- Access to the imaging data, electrophysiology data, or behavioral data is available from the lead contact upon request. This study analyzes existing, publicly available connectome data; accession information for this dataset is detailed below (Cell type accession) and in the key resources table.
- Original code has been deposited in a Zenodo repository and is publicly available as of the date of publication, indexed in the key resources table.

- The cell types we describe here (PPL2-1, PPL2-3, PPM1/2-1) are named in public databases as follows. The hemibrain:v1.2 dataset (https://neuprint.janelia.org) refers to these cells as PPL201, PPL203, and PPM1201. Virtual Fly Brain (https://www.virtualflybrain.org/) contains exemplars of each cell type, e.g. vfb_00013578, vfb_00013528, and vfb_00013337. FlyCircuit (https://www.flycircuit.tw/) refers to these same exemplars as TH-F-000011, TH-F-300052, and TH-F-000005. In a published collection of *Drosophila* dopamine neuron transgenic lines,[4] these cells are referred to as LH-CA, SLP, and VLP-SAD.

EXPERIMENTAL MODEL AND SUBJECT DETAILS

Fly husbandry and genotypes

Flies were raised on cornmeal-molasses food (New Brown 19L, Archon Scientific) or Nutri-Fly GF German food (Genesee Scientific) in an incubator on a 12-hour/12-hour light/dark cycle at 25° C at 50-70% relative humidity.

Genotypes of flies used in each figure are as follows:

for imaging from PPM1/2-1 and PPM1/2-3 in Figures 2B–2G, 3B, 4A, 4B, S2, and S3A:

w⁻/w⁻; TH-D-AD #1 / P{20XUAS-IVS-Syn21-opGCaMP6s-P10}su(Hw)attP5; 61H03-DBD #1 (attP2) / + except one experiment which used *w⁻/w⁻; TH-D-AD #1 / TH-G-KZ #1 (JK22C); 61H03-DBD #1 (attP2) / P{20XUAS-IVS-Syn21-OpGCaMP6s-p10}su(Hw) attP1* for imaging from PPL2-1 in Figures 2C, 2D, 2F, 2G, 3D (responses to EtOH), 4C, 4E, S2, S3A, and S3B:

w⁻ / w⁻; {pJFRC7-20XUAS-cyRFP}VK00037 / +; TH-C′-Gal4 / PBac{y[+t7.7]w[+mC]=20XUAS-IVS-jGCaMP7f}VK00005

for imaging PPL2-1 in Figure 3D (responses to vinegar) and Figure S3B:

+ / *w⁻; {pJFRC7-20XUAS-cyRFP}VK00037* / +; *TH-C′-Gal4 / PBac{y[+t7.7]w[+mC]=20XUAS-IVS-jGCaMP7f}VK00005* for imaging from PPL2-3 (Figures 2C, 2D, 2F, 2G, 3F, 3G, 4D, 4F, S2, and S3):

w⁻/w⁻; 76F02-AD #B (attP40w) / P{20XUAS-IVS-Syn21-opGCaMP6s-P10}su(Hw)attP5; 55C10-DBD #1 (attP2)/ +

for patch-clamp recordings from PPM1/2-1, PPL2-1, and PPL2-3 in Figures 3A, 3C, and 3E:

w⁻/w⁻; +/+; P{20XUAS-IVS-mCD8::GFP}attp2 / P{w[+mC]=ple-Gal4.F}3

We found that the split-Gal4 combination *TH-D-AD #1; 61H03-DBD #1 (attP2)* targets several dopaminergic neurons in the PPM2, PPL2c, and PPL1 clusters. We used this line to drive GCaMP expression in PPM1/2-1 and PPM1/2-3 neurons. (Note that PPM1/2-3 neurons appear only in Figure S4B.)

We found that the split-Gal4 combination *76F02-AD #B (attP40w); 55C10-DBD #1 (attP2)* targets several dopaminergic neurons in the PPL2ab and PPL1 clusters. We used this line to drive GCaMP expression in PPL2-3 neurons. This line consistently labels PPL2-3, although this labeling was not noted in a previous report (where PPL2-3 is called "SLP").[4]

TH-C′-Gal4 targets a large subset of dopamine neurons.[4] One of the cells targeted by this driver is PPL2-1, and this is the only neuron targeted by this driver that arborizes in the central lateral horn. Therefore, by analyzing fluorescence specifically in the central lateral horn, we could use this line to measure activity in PPL2-1 neurons.

These genetic driver lines allowed us to isolate GCaMP signals from individual cell types by analyzing regions of interest (ROIs) that were specific to the neuron in question. We found that different arbors within the same neuron generally had highly correlated activity, and so we can use an ROI targeted to one arbor to infer the activity of the cell as a whole.

ple-Gal4 targets a large subset of dopaminergic neurons. We used it to target PPL2ab and PPM1/2 neurons for electrophysiology experiments. The identity of these cells was determined by filling the cell with biocytin or neurobiotin via the patch pipette and then performing immunostaining *post hoc*.

Fly preparation and dissection

All experiments were performed on female flies 12-24 hours (for electrophysiology) or 24-48 hours (for imaging) post-eclosion, except for a small number of imaging experiments which used slightly older flies (48-96 hours post-eclosion). In some imaging experiments (4 of 8 PPM1/2-1 experiments and 19 of 48 PPL2-3 experiments), flies were deprived of food (but not water) for 12-24 hours prior to the experiment to promote walking behavior. Because we had a large number of starved and also non-starved flies for PPL2-3 experiments, we were able to perform a quantitative comparison of locomotor responses and odor responses in starvard versus non-starved flies for this cell type; this analysis showed no systematic effect of starvation. No circadian restriction was imposed for the time of experiments.

Flies were briefly cold anesthetized prior to dissection. For electrophysiology experiments, the preparation holder consisted of flat steel foil secured to an acrylic platform with the foil oriented parallel to the horizontal body plane, with the fly's head and thorax inserted gently partway through a hole in the foil. Imaging experiments either used a similar steel holder, or else a 3D-printed holder (Form 2 with Grey Pro and Rigid resin, Formlabs) in order to expose a larger surface of the fly's eye below the holder. The fly was secured in the holder using UV-curable glue (Loctite AA 2972) and cured with a brief (<1 sec) pulse of ultraviolet light (LED-200, Electro-Lite Co). To eliminate large brain movements, muscle 16 was removed and the proboscis was either glued in place or the proboscis extension muscles carefully transected with fine forceps (Dumont #5). After covering the dorsal surface of the head in saline, a hole was cut in the head capsule and some trachea and muscles removed as necessary to expose the brain region of interest. For electrophysiology experiments, an aperture was made in the perineural sheath around the cells of interest using fine forceps. The external solution contained (in mM): 103 NaCl, 3 KCl, 5 N-tris(hydroxymethyl) methyl-2-aminoethane-sulfonic acid, 8 trehalose, 10 glucose, 26 $NaHCO_3$, 1 NaH_2PO_4, 1.5 $CaCl_2$ and 4 $MgCl_2$, with osmolarity adjusted to 270–273 mOsm and a pH of 7.3 when bubbled

with 95% O_2, 5% CO_2. External solution was continuously perfused over the brain during electrophysiology and until just before the start of imaging acquisitions.

METHOD DETAILS

Patch-clamp recordings

Patch pipettes made from filamented borosilicate glass (OD 1.5, ID 0.86 mm, Sutter) using a P-97 Sutter puller and then fire-polished using a microforge (ALA Scientific Instruments) to achieve a final resistance of 8-12 MOhm. The internal solution contained (in mM): 140 potassium aspartate, 10 HEPES, 4 MgATP, 0.5 Na3GTP, 1 EGTA, 1 KCl and 15 neurobiotin citrate (Vector labs), filtered through a 0.22 uM filter. To visualize cells for recording we used a CMOS camera (GS3-U3-51S5M-C, FLIR) mounted on an upright compound microscope (Olympus BX51WI) with a 40x water immersion objective (UPlanFL, Olympus). We used a 100-W Hg arc lamp (U-LH100HG, Olympus) and an eGFP longpass filter (U-N41012, Chroma) to detect GFP fluorescence. The fly was illuminated from below using bright-field transmitted light through the microscope condenser. Recordings were obtained using an Axopatch 200B amplifier and a CV-203BU headstage (Molecular Devices). Voltage signals were low-pass filtered at 5 kHz before acquiring at 20 kHz on a National Instruments USB-6343 DAQ. To counteract leak currents caused by the recording electrode, at the start of each experiment we applied a constant hyperpolarizing current that lowered the membrane potential by ~5mV; this hyperpolarizing current was then applied constantly for the full duration of the recording.[68] The liquid junction potential was corrected post hoc by subtracting 13 mV from recorded voltages.[68] In electrophysiological experiments,we recorded one cell per fly.

Two-photon calcium imaging

Imaging experiments were performed using a galvo-resonant two-photon microscope with a movable stage (Thorlabs Bergamo II), a 20×/1.0 NA objective (XLUMPLFLN20XW, Olympus), and a fast piezoelectric objective scanner (Physik Instrumente P725) for volumetric imaging. We used a Chameleon Vision-S Ti-Sapphire femtosecond laser tuned to 940 nm for two-photon excitation of GCaMP. Emission fluorescence was collected on a GaAsP PMT (Hamamatsu) through a 525-nm bandpass filter (MDF-QUAD2, Thorlabs). We used ScanImage 2018 software (Vidrio Technologies) and custom Matlab scripts to control the microscope and collected the imaging data using National Instruments PXIe-6341 hardware.

In most experiments the imaging region was 256×128 pixels, with 12 slices in the *z*-axis for each volume (6-12 μM per slice) resulting in a 6-7 Hz volumetric scanning rate. In a few cases (namely the PPL2-1 imaging experiments in Figures 2C, 2D, 2F, 2G, 3D (EtOH only), 4C, 4E, and S2), we used a volume consisting of 4-6 512×256 imaging planes instead, with approximately the same volume rate.

Measurement of fly locomotion

The fly stood on a 9-mm ball made of white foam (FR-4615, General Plastics) painted with black shapes. The ball floated above a 3D printed plenum made of clear or white acrylic (Autotiv). Medical-grade breathing air flowed into the base of the plenum and out into a hemispherical depression to suspend the ball while allowing it to rotate freely. The ball was illuminated by two round boards of 36 IR LED lamps (SODIAL). The movement of the ball was tracked at either ~60 Hz (PPL2-1 data in Figures 2C, 2D, 2F, 2G, 3D (EtOH only), 4C, 4E, and S2) or 25 Hz (all other experiments) using a CMOS camera (CM-3-U3-13S2M-CS, FLIR) fitted with a Tamron 23FM08L 8-mm 1:1.4 macro zoom lens and an 875 nm shortpass filter (Edmund Optics #86-106) to block out the two-photon laser. Machine vision software (FicTrac[69]) converted the image of the ball to an estimate of the ball's position in all three axes of rotation as well as the fly's fictive 2D position at each time point, and also recorded video of the fly for use in identifying grooming behavior.

Delivery of odor stimuli

In electrophysiology experiments, a stream of medical breathing air (2.5 L/min) was passed through an activated carbon filter and directed at the fly through a carrier tube (4 mm inner diameter) positioned ~1 cm from the front of the fly. A portion of this air stream (12 mL/min) was diverted away from the carrier and directed by 3-way solenoid valve into the headspace of a clean 1.5 mL vial (National Scientific, C4011-5W) containing 200 μL of a 1:100 solution of odor in paraffin oil, or else paraffin oil alone. The solenoid normally directed the odor stream to the empty vial and switched airflow into the odor vial after receiving a command. Valve commands were sent from Matlab via a digital line using a USB-6343 DAQ (National Instruments). After passing through either vial, the odor stream joined the carrier stream again. Paraffin oil was stripped of low–molecular weight volatiles by storing it under negative pressure for at least several days before use.

In most imaging experiments, clean air was passed through an activated carbon filter and directed at the fly through a 19g steel tube placed ~5 mm in front of the fly at 20 mL/min. A solenoid valve switched between this and a parallel air stream that had passed through the headspace of a 1.5 mL vial containing a 1:100 dilution of odor in paraffin oil. CO_2 was presented using a similar system, but diluting the CO_2 in a stream of clean air instead of passing it through an odor vial. In a subset of imaging experiments (PPL2-1 data in Figures 2C, 2D, 2F, 2G, 3D (EtOH only), 4C, 4E, and S2), a wider 4.5 mm odor delivery tube and undiluted ethanol odor stimulus at 12 mL/min were used. Photo-ionization detector (PID) measurements (Aurora Scientific) from the position of the fly confirmed that the intensity and temporal dynamics of the two odor delivery methods were roughly equivalent.

QUANTIFICATION AND STATISTICAL ANALYSIS

Data analysis was performed using Matlab R2016a, R2017b, and 2019b, (MathWorks) and R 3.6.0; the details are described below. Some initial processing of calcium imaging and behavior video data was parallelized on a high-performance computing cluster (Harvard Medical School Research Computing O2 cluster).

Calcium imaging alignment and processing

Rigid motion correction in the *x*- and *y*-axes was performed for each acquisition using the NoRMCorre algorithm.[70] Volumetric ROIs were defined by combining 2D ROIs drawn in multiple imaging planes. Fluorescence values were determined by averaging all pixels in the volumetric ROI. Baseline fluorescence (the denominator F in ΔF/F) was calculated using either the average fluorescence during the pre-stimulus or pre-movement baseline period (Figures 2B–2D, 3B, 3D, 3F, 3G, and S3), the 5th percentile of fluorescence values for an ROI throughout the entire experiment (Figures 2E–2G and S2), or the average the 5th percentile of fluorescence values within a sliding 60-second window centered on each time point (Figure 4). For display purposes, ΔF/F traces in all figures were smoothed with a Gaussian kernel 3 samples wide.

Electrophysiology spike detection

In whole-cell recording data, spikes were identified by setting a threshold on the second derivative of the recorded voltage signal.

Morphology and connectomics analysis

All connectomic data were obtained from the hemibrain:v1.2 dataset.[32] Synapse counts in each brain region (Figures 1D–1F) were obtained by downloading the data from neuprint[71] (https://neuprint.janelia.org) using a custom Neo4j Cypher query. Example neuron morphologies (Figure 1A) were created by capturing a 2D projection of each neuron from the hemibrain:v1.2 dataset and converting it to a silhouette using ImageJ[72] 1.52. Segregation indices (Table S1) were calculated in R using the flow_centrality() function from the neuprintr and hemibrainr packages.[73,74] Identity, cell type, and connection strength of upstream and downstream synaptic partners (Table S2; Figures 1G–1K) were obtained in R, again using the neuprintr and hemibrainr packages. Only partners that were fully traced were included in the analysis. For the connectivity similarity plots in Figure S1, connectivity data was obtained as described above and the pairwise cosine similarity between all upstream or downstream partners was calculated for each neuron, using the number of synapses made with each partner as the connection strength.

Locomotion data processing

The displacement of the spherical treadmill in each of the three axes of rotation as well as the fly's fictive 2D position (in the *xy* plane) was computed by FicTrac online or post hoc using recorded video of the treadmill. Then, the fly's translational (*xy*) walking speed was calculated by taking the difference in fictive 2D position between consecutive time points. These speed measurements were smoothed repeatedly 10 times with a Gaussian kernel 7 (60 Hz sampling) or 5 (25 Hz sampling) samples in width, then downsampled to match the volume rate of the imaging data. Finally, the speed data was shifted back two imaging volumes (~300 ms) in time, chosen because this maximized the correlation between the two signals. For the binned walking speed analysis (Figure 2F) the ΔF/F data for a given experiment was sorted into 45 bins based on the fly's current walking speed, and the mean ΔF/F within each bin was calculated. Bin widths and edges were chosen by sorting the walking speed data and then dividing it into bins that each contained the same number of datapoints using custom MATLAB code. Locomotion and grooming epochs (Figures 2C, 2D, and S3) were detected in a semi-automated fashion using the mean optic flow (calculated using the estimateFlow() function from Matlab's machine vision toolbox) in each of two ROIs around the fly and the spherical treadmill, respectively, in the video of the fly's behavior. All grooming epochs were further verified by manual inspection to distinguish them from other non-locomotor leg or wing movements. Cross-correlation coefficients between walking speed and ΔF/F (Figure 2C) were calculated and normalized using Matlab's xcorr(). In pilot analyses, when we explored the effect of using rotational velocity as a predictive variable, we found that it explained almost none of the variance in neural activity that was not already explained by 2D walking speed.

Modeling PPM1/2-1 activity

For the PPM1/2-1 model (Figures 4A and 4B), we first processed locomotion data as described above, and smoothed and z-scored ΔF/F data with a Gaussian kernel 3 samples wide. Estimated odor responses were calculated by convolving the trial-averaged odor response in the single PPM1/2-1 cell that responded to the odor stimulus with the command signal used to activate the odor valve. Individual models for each experiment were fit using the stepwiselm() function from Matlab's statistics toolbox and inputs consisting of walking speed and estimated odor responses, with an adjusted R^2 threshold of 0.03 to add a term to the model. The models for seven of the eight flies were not improved by inclusion of the odor term and therefore did not include it in their stepwise models.

Modeling PPL2-1 and PPL2-3 activity

The PPL2-1 and PPL2-3 models were fit using the lsqcurvefit() function from Matlab's optimization toolbox. The full model design used walking speed, estimated odor responses, and the timing of odor delivery to predict z-scored ΔF/F. Walking data was processed as described above. The odor response kernel for each experiment was generated by using Matlab's fit() function to fit an 8th-order Fourier function to ΔF/F in an 18-sec window after all odor presentations from the low-density odor blocks of each

experiment. The kernel was then convolved with the onset of each odor stimulus to generate an estimated odor response term. To model odor-dependent subtractive inhibition, the time-integrated history of odor delivery for each time point was also calculated by integrating the total time in which the odor valve was open in the past 240 sec multiplied by a difference of exponentials function with an onset time constant of 0.5 sec and a decay time constant of 175 sec.

$$f(x) = e^{\left(\frac{-x}{\tau_1}\right)} - e^{\left(\frac{-x}{\tau_2}\right)}$$

To model suppression of the odor response, we used an approach that has been used to model short-term synaptic depression.[75,76] Specifically, the odor response term (f_{odor}) was multiplied by a constant scaling factor F ($0 < F < 1$) at the onset of each odor stimulus, recovering exponentially towards baseline with a time constant of 150 sec. The parameters fit for each model consisted of the adaptation scaling factor F, an intercept term C, and the coefficients for the linear terms of walking speed, modeled odor response (with suppression), and subtractive inhibition calculated from the integrated odor history.

$$\hat{y} = \beta_1(f_{odor}) + \beta_2(speed) + \beta_3(subtractive\ inhibition) + C$$

Model performance was evaluated and R^2 values and 95% confidence intervals for each model were calculated using a bootstrapping approach with an 80%/20% train/test split and n=1000 iterations. Alternative models used for the comparisons in Figures 4E and 4F were obtained using the same protocol, but without either the subtractive inhibition term, the suppression of the odor response term, or both.

To quantify the suppressive effect of repeated odor pulses for each PPL2-1 and PPL2-3 experiment, we first quantified the predicted ΔF/F due to locomotor speed, and we subtracted this from the measured ΔF/F to account for the contribution of locomotion. Then, we measured the peak ΔF/F during a 2-sec window after each of the first 5 odor pulses. Finally, we normalized these values by the magnitude of the first peak.

Current Biology, Volume *32*

Supplemental Information

Locomotor and olfactory responses in dopamine neurons of the *Drosophila* superior-lateral brain

Michael Marquis and Rachel I. Wilson

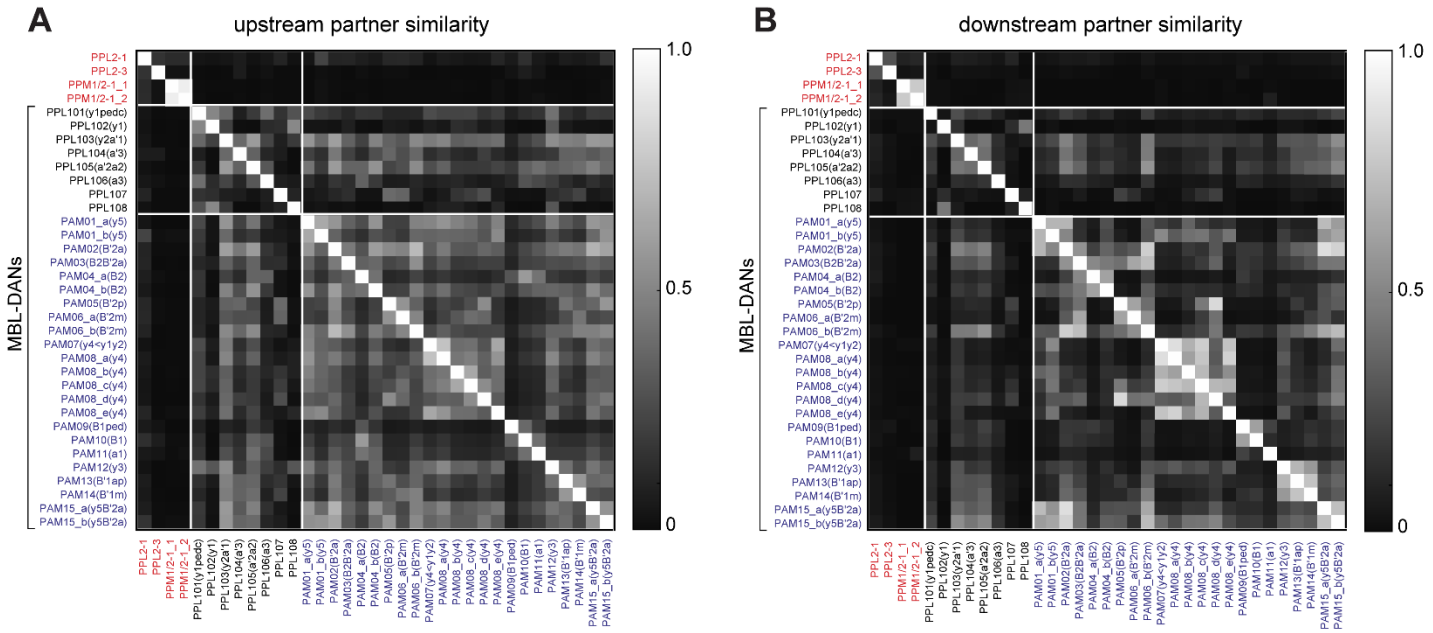

Figure S1. Comparing PPM1/2-1, PPL2-3, PPL2-1, and mushroom body lobe dopamine neuron connectivity, related to Figure 1.

A. Heatmap showing pairwise cosine similarity scores between neurons, based on the identity and synaptic connectivity of their upstream partners in the hemibrain v1.2 dataset. Note that PPM1/2-1, PPL2-3, PPL2-1 (red) are dissimilar from each other, and also from mushroom body lobe dopamine neurons (MBL-DANs).

B. Same as in A, but for connectivity with downstream instead of upstream partners.

The fact that these three superior brain dopamine neurons have such dissimilar patterns of connectivity is not surprising, as their arbors tile the olfactory regions of the superior brain. Specifically, PPM1/2-1, targets ventral LH/SLP (Figure 1A). Meanwhile, PPL2-1 arborizes in dorsal LH/SLP (Figure 1B). Finally, PPL2-3 arborizes in posterior-dorsal LH/SLP (Figure 1C). The tiled arrangement of these arbors is reminiscent of the way that mushroom body dopamine neurons tile the mushroom body lobes[S1], and it implies that these different LH/SLP dopamine neurons have distinct and spatially segregated synaptic partners.

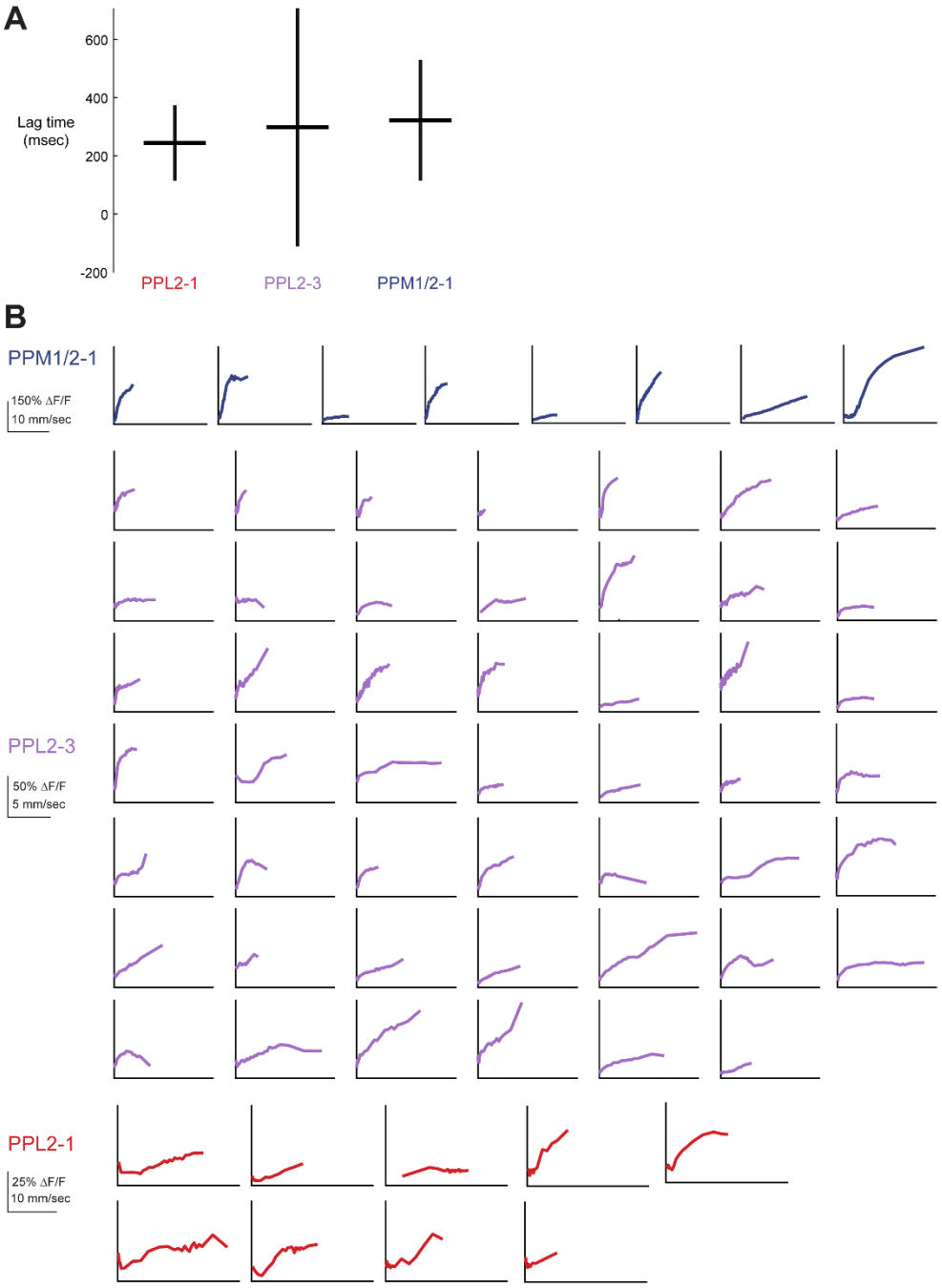

Figure S2. Details of dopamine neuron locomotor responses, related to Figure 2.
A. Average lag between changes in walking speed and recorded ΔF/F in PPM1/2-1, PPL2-3, and PPL2-1 neurons, calculated by finding the number of lag samples that maximized the cross-correlation value between walking speed and ΔF/F, and then dividing that number by the imaging volume rate. Horizontal lines represent the mean for each cell type, and vertical lines show the SD of each group.
B. Binned ΔF/F vs. movement speed plots for individual flies. This shows the same data that is overlaid in Figure 2F, but separated so that each plot shows the data from a single fly.

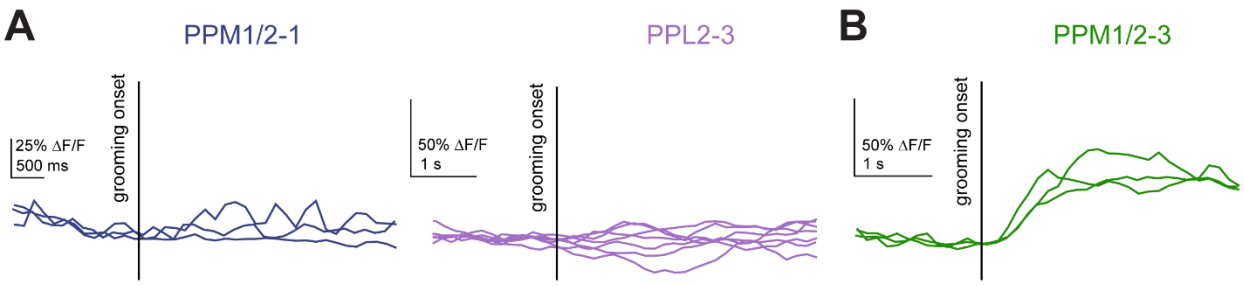

Figure S3. Dopamine neuron activity during grooming, related to Figure 2.
A. Event-averaged GCaMP responses at the onset of grooming bouts, for PPM1/2-1 neurons and PPL2-3 neurons. Each trace is the event-averaged response of one fly. Neither of these cell types was active during grooming. PPL2-1 is omitted here because we did not observe any instances of grooming during PPL2-1 imaging.
B. Event-averaged GCaMP responses at the onset of grooming bouts for another dopamine neuron called PPM1/2-3 in the hemibrain connectome; this neuron is labeled by the same Gal4 line we used to target PPM1/2-1 neurons, and so it was sometimes included in our imaging volume. These data show that PPM1/2-3 becomes active just after the onset of grooming.

Neuron type	Hemibrain instance	Segregation index
AL-LN	lLN2P_a(Patchy)_R	3e-4
PPM1/2-1	PPM1201_R	0.019
PPL2-3	PPL203_R	0.023
AL-LN	lLN15_R	0.025
AL-LN	vLN25	0.046
PAM-DAN	PAM04_a(B2)_R	0.064
PPM1/2-1	PPM1201_R	0.068
EPG	EPG(PB08)_R4	0.073
EPG	EPG(PB08)_R3	0.082
LH-ON	LHPV5a1_a_R	0.127
LH-ON	LHPV5g1_a_R	0.136
PPL2-1	PPL201_R	0.139
LH-ON	LHAD1a2_b_R	0.150
EPG	EPG(PB08)_R3	0.152
PAM-DAN	PAM08_b(y4)_R	0.174
PAM-DAN	PAM05(B'2p)_R	0.197
AL-PN	DM4_adPN_R	0.260
AL-PN	DM3_adPN_R	0.272
PFL-1	PFL1(PB12a)_L2_C3	0.798
PFL-1	PFL1(PB12a)_L5_C6	0.838

Table S1: Polarization of LH/SLP dopamine neurons versus other *Drosophila* neurons, related to Figure 1.

Segregation index[S2] indicating the degree of polarization of the dopamine neurons (DANs) in this study and a number of comparison neurons in the hemibrain:v1.2 dataset[S3]. A higher score indicates a greater degree of separation between the cell's inputs and outputs. The DANs focused on in this study are shown in blue. Cell types for comparison were chosen to represent a diversity of morphologies, including some well-studied cell types.

Neuron type	Hemibrain instance	% synapses w/top 10 downstream partners	% synapses w/top 10 upstream partners
PPM1/2-1	PPM1201_R	6	23
PPM1/2-1	PPM1201_R	6	27
PPL2-3	PPL203_R	8	19
PPL2-1	PPL201_R	9	17
LH-ON	LHAD1a2_b_R	28	35
AL-LN	lLN15_R	42	45
LH-ON	LHPV5a1_a_R	43	38
LH-ON	LHPV5g1_a_R	48	50
AL-LN	lLN2P_a(Patchy)_R	48	51
AL-LN	vLN25	60	48
AL-PN	DM4_adPN_R	61	70
AL-PN	DM3_adPN_R	61	50
EPG	EPG(PB08)_R3	73	55
EPG	EPG(PB08)_R3	73	58
EPG	EPG(PB08)_R4	74	63
PFL-1	PFL1(PB12a)_L2_C3	79	81
PFL-1	PFL1(PB12a)_L5_C6	83	81
PAM-DAN	PAM08_b(y4)_R	84	60
PAM-DAN	PAM05(B'2p)_R	90	57
PAM-DAN	PAM04_a(B2)_R	97	78

Table S2: High convergence and divergence of LH/SLP dopamine neuron connectivity versus other *Drosophila* neurons, related to Figure 1.

This table shows the percentage of all the cell's input or output synapses that are made with the top 10 most strongly connected upstream or downstream partners. For LH/SLP dopamine neurons, a relatively small percentage of their synapses are made with their top synaptic partners, indicating high convergence and high divergence. Data are taken from the hemibrain:v1.2 dataset[S3].

AL-PN = antennal lobe projection neuron, EPG = central complex compass neuron, LH-ON = lateral horn output neuron, PAM-DAN = mushroom body lobe dopamine neuron of the PAM cluster, PFL = PFL1 neuron, AL-LN = antennal lobe local neuron.

Supplemental References

S1. Aso, Y., Hattori, D., Yu, Y., Johnston, R.M., Iyer, N.A., Ngo, T.-T.B., Dionne, H., Abbott, L.F., Axel, R., Tanimoto, H., et al. (2014). The neuronal architecture of the mushroom body provides a logic for associative learning. eLife *3*, e04577.

S2. Schneider-Mizell, C.M., Gerhard, S., Longair, M., Kazimiers, T., Li, F., Zwart, M.F., Champion, A., Midgley, F.M., Fetter, R.D., Saalfeld, S., et al. (2016). Quantitative neuroanatomy for connectomics in Drosophila. eLife *5*. 10.7554/eLife.12059.

S3. Scheffer, L.K., Xu, C.S., Januszewski, M., Lu, Z., Takemura, S.Y., Hayworth, K.J., Huang, G.B., Shinomiya, K., Maitlin-Shepard, J., Berg, S., et al. (2020). A connectome and analysis of the adult Drosophila central brain. eLife *9*. 10.7554/eLife.57443.